Eur. Phys. J. Plus (2023) 138:565
https://doi.org/10.1140/epjp/s13360-023-04204-w

THE EUROPEAN PHYSICAL JOURNAL PLUS

Regular Article

# Full spectral coverage generation for calibration of astronomical telescope spectrographs

**Yang Wang**[a], **Lei Xie, Long Chen, Qinning Sun, Fengrong Zhu**

School of Physical Science and Technology, Southwest Jiaotong University, Chengdu 611756, China

Received: 17 January 2023 / Accepted: 17 June 2023
© The Author(s), under exclusive licence to Società Italiana di Fisica and Springer-Verlag GmbH Germany, part of Springer Nature 2023

**Abstract** Calibrating astronomical telescopes necessitates a broadband spectrum that extends into the mid-infrared region, as well as pulse energy that attains magnitudes of tens of μJ while maintaining a stabilized carrier-envelope phase. To address these challenges simultaneously, we introduce a novel and uncomplicated experimental setup that utilizes a specifically oriented type-I bismuth borate crystal. This cost-effective architecture generates pulses that span from 450 to 3000 nm through the combined use of intra-pulse difference frequency generation and optical parametric amplification. The octave-spanning pulses were automatically carrier-envelope phase-stabilized due to self-cancellation of carrier-envelope phase fluctuation. The idler pulse energy achieved was up to 30 μJ without extra amplification stages. By means of our theoretical simulation, this approach exhibits the potential to broaden the spectrum up to 5 μm.

## 1 Introduction

In recently two decades, the emerging astrophotonics focuses on the development of astronomical instrumentation, including fibers and photonic lanterns, fiber Bragg gratings, spectrographs and frequency references, coronagraphy, interferometry and high angular resolution imaging, on ground and in space [1]. The availability of a broad wavelength range is one of the limits for these applications in guiding, shaping, and manipulating the light coming from telescopes. For instance, solar spectroscopy covering from 200 to 2400 nm is frequently implemented to detect plasma dynamics through Doppler shift of spectral lines with well-calibrated instruments [2]. High-resolution astronomical telescope spectrographs are crucial to multiple areas of astrophysics, enabling major breakthroughs such as the discovery and detection of exoplanets similar to the Sun [3]. As the field of astronomy continues to advance, there is an increasing demand for high-precision spectrographs that can provide accurate measurements of celestial objects [4]. To meet this demand, a new generation of precision spectrographs, including CARMENES [5], ESPRESSO [6], and HIRES [7], has been developed. These precision spectrographs are essential for upcoming experiments that are planned for the European Extremely Large Telescope (E-ELT), the Very Large Telescope (VLT), and other projects [8]. These experiments require an absolute calibration with an equivalent Doppler precision of ~2 cm/s, necessitating a highly stable wavelength reference for spectrograph calibration [9]. Moreover, the high-resolution spectrograph apparatus in E-ELT requires an extremely stable wavelength reference and a wavelength coverage from 350 to 2400 nm [10].

In the past, lamps were used for astronomical spectrograph calibration. In order to measure thousands of stellar lines simultaneously, a bandwidth of several hundred nanometers is necessary for astrophysical spectrographs [11]. Thus, owing to a limited coverage, lamps are replaced by laser frequency combs, consisting of equal spacing laser modes in the frequency domain [12]. Frequency laser combs are highly stable and can provide a much larger number of uniformly-spaced, bright, and narrow lines [13]. This enables more accurate calibration of the spectrograph, resulting in higher precision measurements of celestial objects. Despite their advantages, the development of astrocombs faces multiple technical challenges, including the need for comb-lines ranging from 380 (Ca II H and K lines) to 2.4 μm (CO band at 2.3 μm). Wide spectral coverage is therefore a significant challenge for astrocomb development. A laser frequency comb is a powerful tool that generates an enormous amount of narrow, equal-spacing optical modes with frequencies given by $f_m = m f_{REP} + f_{CEO}$, where $m$ is a large integer, $f_{REP}$ is the mode spacing and $f_{CEO}$ is a carrier-envelope offset frequency [14]. Stabilization of both $f_{REP}$ and $f_{CEO}$ is crucial to provide a set of comb lines with well-known frequencies that are traceable to primary standards. Achieving the necessary stability and accuracy of the comb lines requires a stabilized carrier-envelope (CE) phase of the laser pulses [15]. Moreover, to ensure the accurate calibration of astronomical telescopes, it is crucial that the pulse energy attains magnitudes of tens of μJ. For instance, the laser calibration required for the Wide Field

[a] e-mail: yangwang@swjtu.edu.cn (corresponding author)

Published online: 26 June 2023

view Cherenkov Telescope Array (WFCTA) of the Large High Altitude Air Shower Observatory (LHAASO) demands such high pulse energies.[16].

Consequently, the development of an astrocomb laser source faces three key obstacles: achieving broad spectral coverage, stabilizing laser frequency, and attaining pulse energies of approximately μJ. Multiple laser technologies have been proposed for frequency comb stabilization, resulting in competing approaches. Here, we discuss the progress in laser technology development for frequency comb stabilization.

### 1.1 Fiber laser combs

Fiber laser frequency combs have emerged as a compact and robust solution for a wide range of scientific and technological applications. Several recent studies have focused on developing and optimizing these combs to achieve greater stability, precision, and spectral bandwidth. One such study, conducted by Hartl et al., involved the development of a Fabry–Pérot cavity, passively saturable absorber-mode-locked Yb-fiber femtosecond oscillator [17]. This device exhibited a broadened spectrum spanning from 1000 to 1070 nm, as well as a self-referenced $f$-$2f$ $f_{CEO}$ stabilization mechanism. Another study, conducted by Chen et al., focused on a fundamentally mode-locked, femtosecond (206 fs) Yb-fiber laser with an optical spectrum ranging from 1005 to 1045 nm [18]. Xu et al. presented a fully stabilized, self-referenced Yb:fiber frequency comb without the need for additional amplifiers and compressors [19]. The device achieved a maximal spectral bandwidth at the full-width-half-maximum (FWHM) that was close to 27 nm. Martinez et al. demonstrated self-starting, passively mode-locked laser operation in a fiber Fabry-Pérot laser configuration, achieving a spectrum from 1575 to 1625 nm [20]. Wu et al. generated a broadband spectral coverage from 445 to 1450 nm that covers full spectral range of the Keck Planet Finder (KPF) spectrograph [21].

### 1.2 Solid-state laser combs

Solid-state systems have become increasingly popular for their ability to generate shorter pulses and higher average powers directly from the oscillator. Recent studies have focused on optimizing and stabilizing these systems to achieve greater precision and accuracy in frequency comb generation. One of these studies, by McCracken et al., achieved fully stabilized combs from both the Ti:sapphire laser and the optical parametric oscillator (OPO) with sub-MHz comb-tooth linewidths [22]. Endo et al. reported a Kerr-lens mode-locked Yb:$Lu_2O_3$ ceramic laser that was optimized for comb-resolved broadband spectroscopy [23]. This was achieved by locking both the repetition and offset frequencies, resulting in an optical spectrum spanning from 1000 to 1120 nm. Klenner et al. presented the first stabilization of the frequency comb offset from a diode-pumped gigahertz solid-state laser oscillator [24]. This was achieved through the generation of an octave-spanning supercontinuum from 1020 to 1100 nm in a highly nonlinear fiber. Zaugg et al. presented a self-referenceable frequency comb from a vertical external-cavity surface-emitting laser passively mode-locked with a semiconductor saturable absorber mirror [25]. The optical spectrum was centered at 1038 nm, with a bandwidth ranging from 1020 to 1050 nm. Johnson et al. demonstrate the generation of a supercontinuum spanning from 670 to 1750 nm with a pulse energy of ~ 36 pJ using a diode-pumped ytterbium laser and a Yb:$CaAlGdO_4$ laser [26]. This represents an important step forward in the development of high-performance frequency combs using solid-state systems.

### 1.3 Electro-optically modulated laser combs

Electro-optically modulated (EOM) frequency combs represent an alternative approach to achieving the optimal mode spacing required for frequency comb generation. Recent studies have focused on investigating the characteristics and performance of these systems. Ishizawa et al. conducted a study to investigate the phase-noise characteristics of both a phase/intensity-modulated laser with 25-GHz mode spacing and a mode-locked fiber laser with carrier-envelope-offset (CEO) locking [27]. The experimental optical spectrum of the resulting optical frequency comb spanned from 1540 to 1565 nm, demonstrating the potential for high-performance frequency combs using EOM techniques. Beha et al. reported a method for measuring the frequency of continuous-wave laser light using optical-phase modulation [28]. This electro-optic modulation frequency comb produces a supercontinuum with a bandwidth of 20 nm. Kashiwagi et al. used electro-optic modulation and line-by-line pulse synthesis to generate the spectral broadening from 1040 to 1750 nm [29]. These studies represent important advances in the development and optimization of EOM frequency combs, offering a promising alternative to traditional frequency comb generation techniques [30].

### 1.4 Chip-scale frequency laser combs

Microresonators are highly promising chip-scale devices that leverage the nonlinear Kerr effect in a dielectric medium to generate multi-GHz line spacings without the need for filtering. Del'Haye et al. demonstrated $f$-$2f$ self-referencing of a microresonator-based optical frequency comb with an octave-spanning microcomb spectrum centered at a wavelength of 1.11 μm, with a resolution bandwidth of 5 GHz [31]. Mayer et al. showed the first carrier-envelope-offset detection of a mode-locked laser based on supercontinuum generation from 1000 to 1200 nm in a $Si_3N_4$ waveguide [32]. Obrzud et al. used a ring-type silicon nitride microresonator to provide lines from 1450 to 1700 nm resolved by the spectrometer [33]. These studies demonstrated the significant potential

of microresonator-based frequency combs, offering a compact solution for spectrograph calibration. While high pulse energy is desirable for astronomical telescope spectrograph calibration, there is a drawback in that it may not provide full spectral coverage.

### 1.5 Ancillary astrocomb

Astrocombs, which are critical for spectrograph calibration in astronomical telescopes, often require ancillary components to achieve the desired spectral coverage and mode spacing. Ycas et al. described and characterized a 25 GHz laser frequency comb based on a cavity-filtered erbium fiber mode-locked laser by Fabry–Pérot etalons [34]. The resulting comb provides a uniform array of optical frequencies spanning from 1450 to 1700 nm. Tang et al. reported a thermally stabilized fiber Fabry–Pérot etalon as a wavelength calibrator for high-precision spectroscopy from 650 to 900 nm [35]. Glenday et al. developed and successfully operated a green astrocomb with 16 GHz spectral line spacing from 500 to 620 nm [36]. Gambetta et al. reported their work in manipulating the supercontinuum and modifying the phase-matching angle in the nonlinear crystal to obtain broadly tunable idler pulses of a difference-frequency-generation (DFG) process from 5000 to 12,000 nm [37]. However, the pulse energy was approximately 1 pJ, which falls short of the requisite strength for effective telescope calibration. Boggio et al. proposed wavelength calibration based on four-wave mixing between two lasers propagating in nonlinear fibers with a spectral range from 1350 to 1900 nm [38]. Cheng et al. demonstrated an optical parametric oscillator-based astrocomb from 1150 to 1800 nm, covering the H and J bands for the Extremely Large Telescope. An independent $f$-to-2$f$ interferometer measurement of $f_{\mathrm{CEO}}$ was applied, since the CE phase was not passively-stabilized [39].

Although mid-infrared pulses can be generated through the DFG process via wave mixing of a supercontinuum, the pulse energy is typically limited to the level of pJ or nJ. In such cases, the generation of mid-infrared typically involves the use of a type-II BIBO or BBO crystal as the nonlinear medium. Notably, this process occurs without the amplification of the idler or signal. As a result, these pulses are commonly employed as seeding pulses, which are then amplified through additional, complex amplification stages. Previous works in this field have been limited in their spectral bandwidth, absence of passively stabilized CE phase, or low pulse energy. In comparison to these earlier studies, we have constructed a simple experimental apparatus to investigate the spectral broadening. Our approach involves a novel technique that utilizes a passive stabilization mechanisms to achieve the desired spectral broadening. By optimizing the pulse energy and the CE phase, we were able to achieve a significant increase in the spectral bandwidth. The octave-spanning mid-infrared pulses were initially generated by intra-pulse DFG in a BIBO crystal. Then, these pulses were amplified in the same crystal by optical parametric amplification (OPA), yielding a pulse energy of ~ 30 μJ without additional amplification stages. At the same time, a new signal was produced as well. Our simple scheme is capable of addressing the spectrograph calibration wavelength coverage for astronomical telescopes, such as ELT. It has the ability to provide wavelengths from near-UV to mid-infrared, including 450–1000 nm (fiber system), 1000–1800 nm (OPA), 1800–3000 nm (DFG and OPA) with passively-stabilized CE phase. Additionally, it can potentially deliver a spectrum spanning from 1800 to 5000 nm with a stable CE phase according to our theoretical simulation.

## 2 Pulse broadening

### 2.1 Principle and setup

Supercontinuum generation is produced in a noble gas filled silica capillary (fiber) with a large diameter mode [40]. This novel approach offers distinct advantages over traditional single-mode optical fibers [41], as the silica capillary fiber has a high-intensity threshold for optical damaging, resulting in high-energy pulses of approximately millijoules. The spectral broadening observed in this study is attributed to the self-phase modulation (SPM) and group velocity dispersion (GVD) that arise during the propagation of laser pulses in the fiber. The selected fiber, provided by Molex LLC, is a polyimide-coated flexible fused-silica capillary tubing with an inner diameter of approximately 500 μm, which is significantly larger than the optical wavelength centered at 800 nm from a Ti:sapphire laser. The $\mathrm{EH}_{11}$ mode dominates in the fiber, with a radial intensity profile that is given by: $I_0(r) = I_0 J_0^2(2.405r/a)$, where $J_0$ is the zero-order Bessel function, $I_0$ is the peak intensity, and $a$ is the capillary radius. With a Gaussian input intensity profile $I_{\mathrm{i}}(r) = I_{\mathrm{i}0}\exp(-2r^2/r_{\mathrm{i}}^2)$, the coupling efficiency of the $\mathrm{EH}_{11}$ mode is maximized under the condition of $r_{\mathrm{i}} = 0.65a$, where $r_{\mathrm{i}}$ and $I_{\mathrm{i}0}$ are the radius and intensity at the entrance of the fiber, respectively. Therefore, great cares were taken to choose the focal length of CM1 as depicted in Fig. 1 to reduce the beam diameter to be ~ 325 μm.

The equation describing propagation of pulse amplitude $A$ is expressed as [42]:

$$\frac{\partial U}{\partial z} + \frac{\alpha}{2} + \frac{i}{2}\beta_2\frac{\partial^2 U}{\partial T^2} - \frac{1}{6}\beta_3\frac{\partial^3 U}{\partial T^3} = i\gamma P_0\left[|U|^2 U + \frac{i}{\omega_0}\frac{\partial}{\partial T}(|U|^2 U)\right], \tag{1}$$

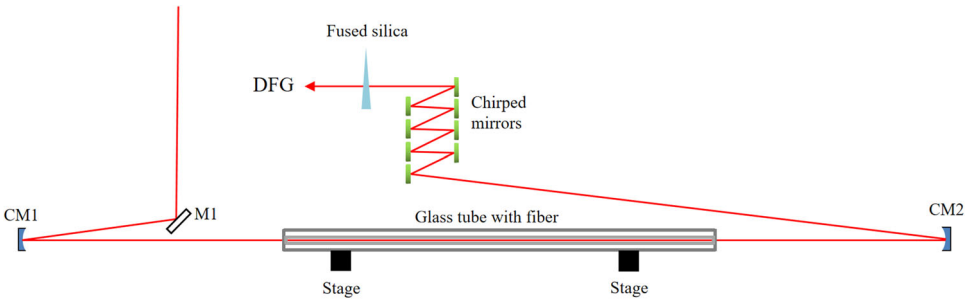


**Fig. 1** The schematic of the spectral broadening and compression setup. M1: dielectric flat mirror; CM1 & CM2: plano-concave mirrors

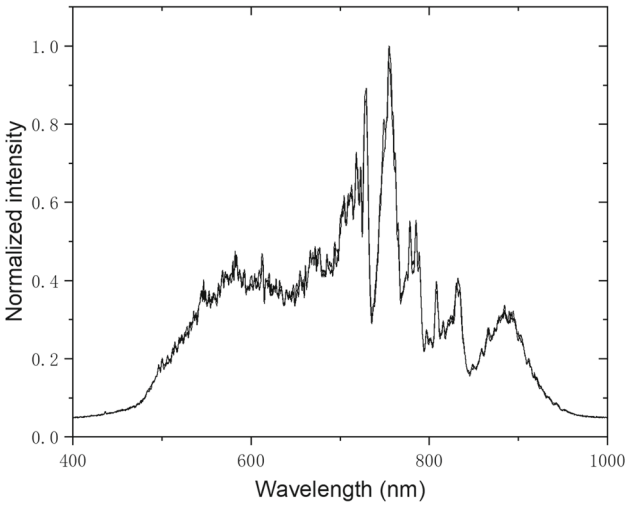


**Fig. 2** The experimental broadening spectrum (supper continuum) after fiber

where $\alpha$ is the field attenuation constant, $U(z, T) = A(z, T)/\sqrt{P_0}$, $P_0$ is the pulse peak power, $T = t - z/v_g$, $v_g$ is the group velocity of the pulse, $\beta_n = \left(\frac{d^n \beta}{d\omega^n}\right)_{\omega=\omega_0}$ (n = 2, 3) and $\omega_0$ is the central frequency. The bandwidth of the pulse is then given by:

$$(\Delta\omega)^2 = \langle\omega^2\rangle - \langle\omega\rangle^2 = \frac{\int \omega^2 |g(\omega)|^2 d\omega}{\int |g(\omega)|^2 d\omega} - \left[\frac{\int \omega |g(\omega)|^2 d\omega}{\int |g(\omega)|^2 d\omega}\right]^2, \quad (2)$$

where $g(\omega)$ is the Fourier transform of $U(T)$.

## 2.2 Results and discussion

In our experiment, a fiber with a length of two meters was filled with neon gas at 25 PSI. The fiber was stretched straight and glued to a plastic piston at each end of a glass tube, as shown in Fig. 1. The piston was secured with glue and two anti-reflection coated windows were used to seal the tube. Besides, gas and vacuum lines, along with a pressure gauge, were connected to the glass tube. Two mechanical stages were employed to adjust the alignment of the fiber horizontally and vertically with respect to the beam pointing. After propagation in the fiber, the outgoing beam was collimated using a plano-concave mirror (CM2). The spectral broadening, ranging from 450 to 950 nm, as illustrated in Fig. 2, was achieved by carefully optimizing the parameters of fiber radius, length, gas species, and pressure. This broadened spectrum supports a Fourier transform limited pulse duration of 2.75 fs, which is very close to a single cycle.

In the experiment, a significant positive group-delay dispersion (GDD) was induced, as displayed in Fig. 3, after propagating a beam in a fiber filled with gas. However, this GDD was later canceled out by utilizing four pairs of chirped mirrors with negative dispersion. The ultra-broadband chirped mirrors, with multi-layer coatings, were able to provide adequate dispersion control over a broad spectral range (450–1000 nm), as demonstrated in Fig. 4 [43]. One pair of chirped mirrors consisted of BK35 and BK38. Slight overcompensation from the chirp mirrors was intentional, as the dispersion from the fiber and chirp mirrors cannot be precisely canceled out. Consequently, a fused-silica wedge providing positive GDD was employed to perfectly eliminate the residual negative GDD by varying its thickness, resulting in desirable pulse compression.

Following compression, the characterization of the pulse was carried out using Second Harmonic Generation Frequency Resolved Optical Gating (SHG-FROG) [44]. The FROG measurement principle and configuration details can be found elsewhere [45]. To automate the recording of the FROG trace, a LabVIEW program was developed. An iterative algorithm was then implemented to retrieve the phase, spectrum, and pulse duration from the FROG trace, as depicted in Fig. 5. By reconstructing the temporal profile

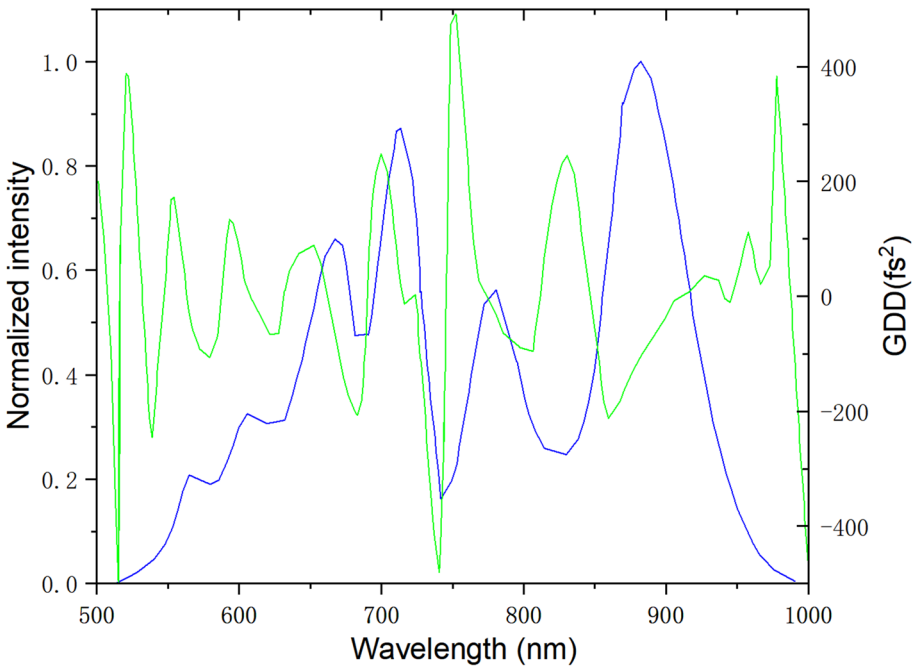


**Fig. 3** The calculated spectral broadening (blue curve) and GDD for different wavelengths (green curve)

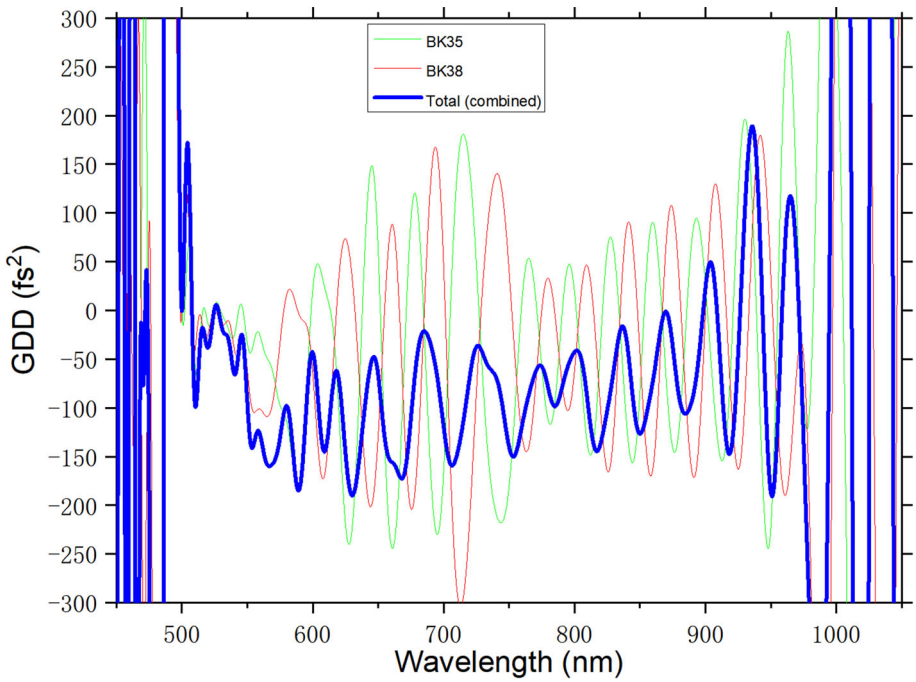


**Fig. 4** The dispersion by a pair of chirped mirrors, consisting of BK35 and BK38. The red curve indicates the GDD from BK38, while the green curve from BK35 and the blue curve represent a total GDD from one pair of chirped mirrors

through the iterative process, a full width at half maximum (FWHM) of 3.8 fs was measured for the pulse duration, with a flat phase indicating a self-consistent and robust result.

## 3 Generation of broadband mid-infrared

### 3.1 Principle of intra-pulse DFG

As one of the most crucial second-order nonlinear effects, DFG has emerged as an attractive and widely used approach for generating infrared radiation due to its continuous wavelength tunability. In this approach, a pulse with an angular frequency of $\omega_p$ is mixed and co-propagates with another pulse with an angular frequency of $\omega_s$ in a nonlinear crystal. This interaction results in the production

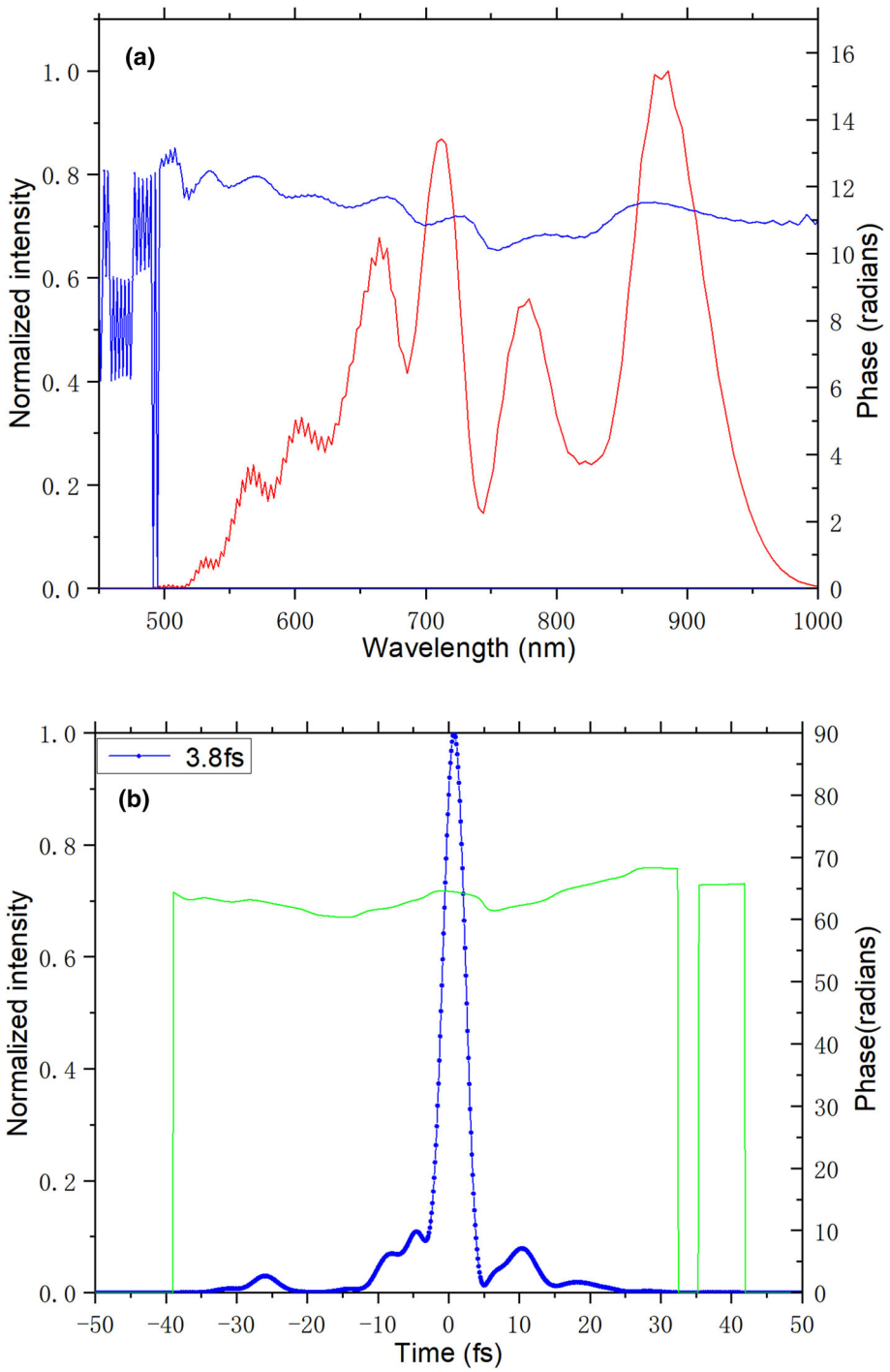


**Fig. 5** **a** The retrieved spectrum (red) and spectral phase (blue), and **b** pulse duration (blue), as well as the temporal phase (green)

of an optical wave with another angular frequency of $\omega_i$, corresponding to the difference between $\omega_p$ and $\omega_s$. The suffixes p, s, and i refer to the pump, signal, and idler pulses, respectively. As a result, the three angular frequencies are determined by the law of conservation of energy, leading to the relation: $\omega_i = \omega_p - \omega_s$. Moreover, the conservation of momentum must be intrinsically satisfied under the phase-matching condition. The wave vector mismatch by the pump, signal, and idler pulses is expressed by:

$$\Delta k = k_p - k_s - k_i, \tag{3}$$

where $k$ denotes the wave vector. Notably, the difference frequency mixing of the pump and signal pulses utilized in our experiment originates from the same laser source, thereby qualifying it as an intra-pulse DFG. This approach confers several advantages, including: (i) support for more than one octave phase-matching bandwidth; (ii) elimination of jitter between the pump and signal;

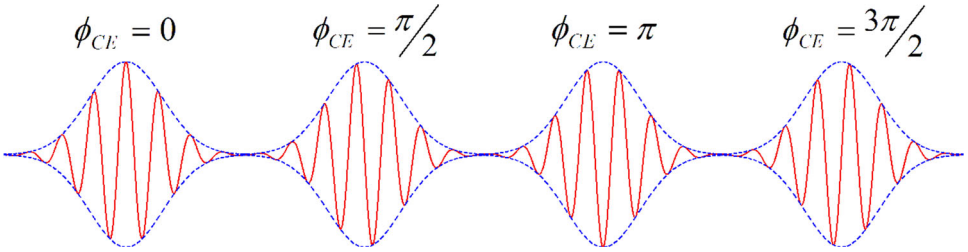


**Fig. 6** The pulses with different CE phase

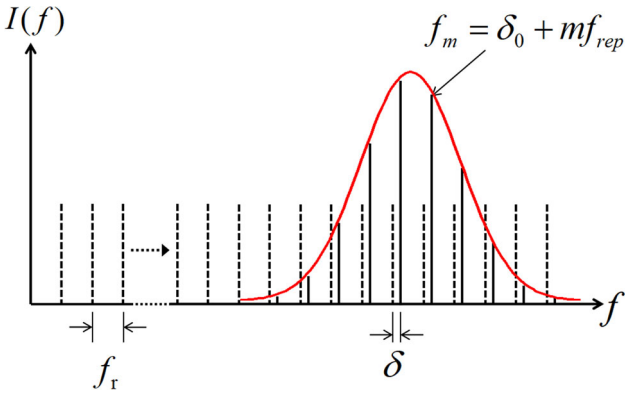


**Fig. 7** Shifted frequency comb. The dashed arrow depicts a large increase in frequency

(iii) automatic stabilization of the CE phase, which will be comprehensively discussed in the next session; and (iv) convenient scaling up of pulse energy to the μJ level without requiring additional amplification stages.

### 3.2 Automatic CE phase stabilization

The stabilization of the CE phase is of paramount importance in laser-frequency-comb calibration for telescopes. One of the key advantages of DFG is the automatic stabilization of the CE phase. The CE phase offset is defined as the relative position difference between the peak of the optical oscillation and the envelope position, as illustrated in Fig. 6. This offset arises from chromatic dispersion caused by a mismatch of the phase group velocity.

The instant electric field of pulse train in frequency domain associated with a fast sinusoidal oscillation (the carrier), and a more slowly varying envelope can be written as [15]:

$$\tilde{E}(\omega) = \exp(i\phi_0)E_0(\omega - \omega_c)\sum_{m=0}^{\infty}\delta(\omega - 2\pi(mf_r + \frac{\Delta\phi_{CE}}{2\pi}f_r)), \tag{4}$$

where σ is defined as $\sigma = -\Delta\phi_{CE}f_r/2\pi$. Here, $E_0$ is the amplitude of the electric field, $\omega_c$ is the carrier frequency, $\phi_0$ is the initial phase, $\Delta\phi_{CE}$ is the CE phase, and $f_r$ is the repetition rate. The optical comb frequency $f_m$ is then determined by:

$$f_m = mf_r + \delta = mf_r - \Delta\phi_{CE}f_r/2\pi \tag{5}$$

The shifted frequency comb is given in Fig. 7 [15].

Thus, the precise calibration of laser frequency combs necessitates the stabilization of the CE phase. The CE phases of the signal, idler, and pump waves are interlinked through the parametric process via the expression: $\Delta\phi_{CEi} = \Delta\phi_{CEp} - \Delta\phi_{CEs}$. If the pump and signal pulses employed in the DFG process originate from the same light source and share the same CE phase ($\Delta\phi_{CEp} = \Delta\phi_{CE0} + C_1$, and $\Delta\phi_{CEs} = \Delta\phi_{CE0} + C_2$), then the CE phase of the idler ($\Delta\phi_{CEi}$) remains constant, as any fluctuations between the pump and idler are automatically nullified. Consequently, the intra-pulse DFG scheme is well-suited for passive CE phase stabilization. In our experiment, the pump and signal are simultaneously derived from short pulses, as shown in Fig. 5. This approach ensures that the idler is CE phase stabilized in a passive and all-optical way.

### 3.3 Choice of crystals

In order to identify the optimal DFG crystal, several key characteristics must be considered. As a nonlinear crystal, the effective optical coefficient is of utmost importance. The crystal must support broadband phase-matching to maximize the intensity of the idler. Furthermore, the conversion efficiency is limited by the spatial walk-off effect that arises from the separation of pump and signal pulses during propagation through the crystal. As such, crystals with a small non-collinear angle are preferred. Another critical prerequisite for crystals is a large transparency range to prevent idler absorption, which could lead to a decline in parametric

**Table 1** Optical properties of nonlinear crystals: BBO, LBO, and BIBO

| Crystals | BBO | LBO | BIBO |
|---|---|---|---|
| NLO coefficient $d_{\text{eff}}$ (pm/V) | 2.2 | 0.85 | 3.2 |
| Damaging threshold (GW/cm$^2$) | >7 | >4.5 | >4.5 |
| Transparency range (nm) | 190–3500 | 160–3200 | 286–2500 |
| Point group | Uniax._(3 m) | Biax._(mm2) | Biax. + (mm2) |

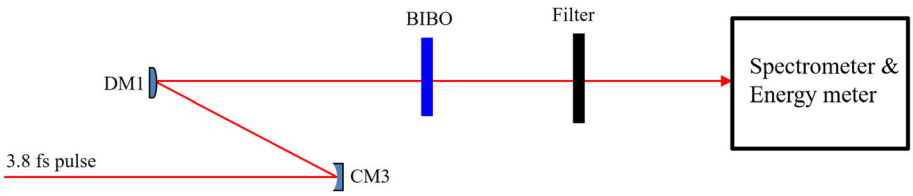


**Fig. 8** The experimental scheme of the intra-pulse DFG. CM3 is a plano-concave mirror and DM1 is a plano-convex mirror

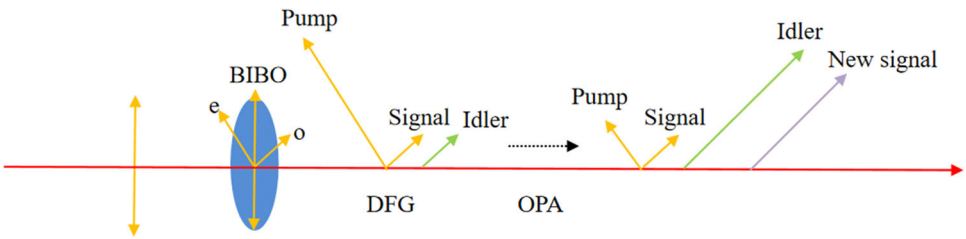


**Fig. 9** A demonstration of two cascaded second-order nonlinear amplification processes in BIBO crystal under phase-matching condition. The new signal was generated by OPA process

amplification. Additionally, crystals should possess a high damaging threshold to facilitate pulse energy scaling, and exhibit low hygroscopicity and a suitable size. Given these stringent requirements, the choices for candidate crystals are rather limited, with only a few crystals, including BBO, BIBO, and LBO, meeting the necessary criteria. The optical properties of these borate crystals are presented in Table 1, which were obtained from crystal manufacturers and references [46–49].

LBO, BBO, and BIBO exhibit a broad phase-matching bandwidth that extends into the near-infrared region, thereby satisfying the aforementioned optical requirements. However, we give preference to BIBO due to its larger effective nonlinear coefficient $d_{\text{eff}}$. Considerable attention was devoted to identifying the optimal cutting angle for phase matching. Ultimately, we selected a type I BIBO crystal with a thickness of 1.5 mm and set the phase-matching angle to 10.7° in the XZ-plane, given that BIBO is a positive biaxial crystal.

## 4 Experimental setup, results and discussion

The laser beam, with an energy of ~ 2 mJ, was focused into the fiber, giving rise to spectral broadening and the generation of an output pulse with an energy of ~ 1.3 mJ. After compression, we employed a plano-concave mirror (CM3, $f = 500$ mm) and a plane-convex mirror (DM1, $f = 150$ mm) to reduce the beam size without introducing dispersion, as demonstrated in Fig. 8.

In this study, two sequential second-order nonlinear processes occurred in a single BIBO crystal. In the first process, intra-pulse DGF transpired between pulses with shorter (pump) and longer (signal) wavelengths generated by the fiber system. The BIBO crystal was oriented appropriately for the phase-matching of the pump and signal pulses. The linearly polarized input pulse was predominantly projected along the e axis, while a small fraction was projected along the o axis, as summarized in Fig. 9.

The principle of cascaded DFG and OPA processes is described in Fig. 10, which provides the conversion efficiency of a 1.5-mm BIBO crystal under phase-matching conditions. This figure allows for the identification of the wavelengths at which DFG and OPA processes occur. The calculation reveals a phase-matching bandwidth spanning from 1000 to 3000 nm, although there is substantial absorption by BIBO beyond 2600 nm. An example demonstrating the signal, pump, and idler generated by intra-pulse DFG under phase-matching conditions is presented below:

$$700.0\ \text{nm}\ (e,\ \text{pump})\ -\ 972.0\ \text{nm}\ (o,\ \text{signal})\ =\ 2500.0\ \text{nm}\ (o,\ \text{idler}).$$

As shown by the left black arrow in Fig. 10, after initiation of intra-pulse DFG, the longer wavelength pulses from fiber will play a role as a pump and thus the idler will be amplified significantly in the following second-order nonlinear process-OPA, while a new signal is concurrently generated. An example of this process under phase-matching conditions, represented by the right black arrow in Fig. 10, is provided below:

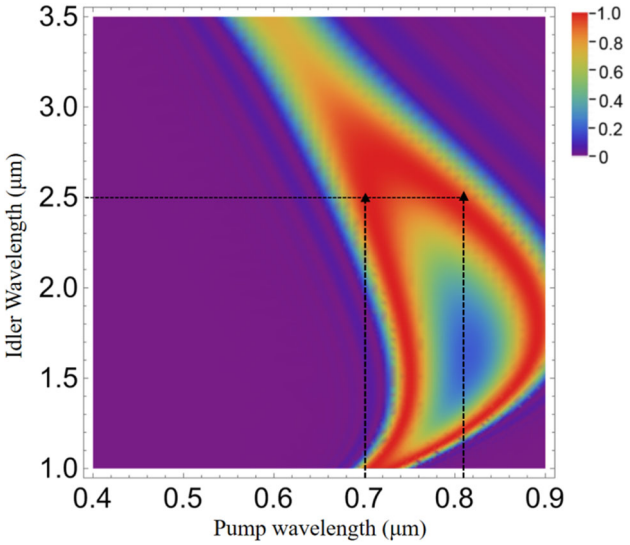


**Fig. 10** The numerical simulation for phase-matching efficiency regarding to pump and idler wavelengths in a 1.5-mm Type I BIBO with a phase-matching angle of 10.7° in the XZ plane

$$810.0\ \text{nm}(e,\ \text{pump}) - 2500.0\ \text{nm}(o,\ \text{idler}) = 1200\ \text{nm}(o,\ \text{signal}).$$

The upper limit of the new signal generated by the OPA process is determined by the wave-mixing of a 900 nm pulse from the fiber and an 1800 nm pulse from the DFG idler, under phase-matching conditions, according to the results in Fig. 10. To maximize the conversion efficiency from pump to idler in the two cascaded processes, the BIBO crystal was carefully oriented, with its e axis oriented at an angle of approximately 9° with respect to the polarization of the input pulses. Consequently, by utilizing an IR spectrometer (C15511-1, Hamamatsu Inc.) with a uncertainty of less than 1%, we were able to observe a near-infrared spectrum ranging from 1.1 μm to 1.8 μm, as measured in Fig. 11a. Furthermore, the octave-spanning spectrum (1.8–3.0 μm) depicted in Fig. 11b originated from the idler in the intra-pulse DFG process, which was subsequently amplified by the cascaded OPA process. Using a long-pass filter, we removed wavelengths less than 1800 nm and employed a pyroelectric energy meter (PE9-ES-C, Ophir Photonics Inc.) to obtain a 30 μJ pulse with a uncertainty of 3%. With a higher pulse energy from the fiber and a larger BIBO crystal, further scaling of the pulse energy is achievable.

In order to extend the idler to the mid-infrared domain, we conducted theoretical simulations. Our findings suggest that a thinner BIBO crystal is capable of supporting a broader range of wavelengths with less walk-off effect. We propose a similar paradigm for laser pulses at mid-infrared wavelengths in a single thin BIBO crystal, achieved via cascaded second-order nonlinear processes of intra-pulse DFG and OPA, as illustrated in Fig. 13. The cutting angle for phase-matching was set at 10.6° in the XZ plane, with a thickness of 0.3 mm. The pump pulse covered a spectral range from 400 to 950 nm, as plotted in Fig. 12. Our simulations indicate that this approach can generate a pulse covering 1.8–5.0 μm. We should emphasize that the wide spectrum generated in the fiber, as recorded in Fig. 2, greatly benefits the mid-infrared pulses spanning to 5.0 μm. This octave-spanning spectrum has numerous potential applications, including laser calibration, astrocombs, and seeding few-cycle mid-infrared high-power lasers. The estimated pulse energy is ~ 5 μJ. This approach is versatile and can also be applied to produce mid-infrared pulses of μJ-level with different wavelengths using other second-order nonlinear crystals, such as KTA, $KNbO_3$, and $LiNbO_3$, due to their relatively large second-order nonlinearity and high damage threshold. These pulses are also expected to have stable CE phase. It is worth noting that one should be mindful of the crystal orientation due to the distinct polarization of pump and signal pulses under phase-matching conditions in different crystals.

Finally, we propose an overall diagram, depicted in Fig. 13. With a higher pulse energy from the laser, a beamsplitter is inserted to divide the supercontinuum from the fiber into two beams: one is used for spectrograph calibration, while the other is utilized for DFG and OPA processes. The output of near- or mid-infrared wavelengths is determined by the choice of the filter. This technique promises full coverage, spanning from 0.45 μm to 5 μm in the future, with the help of a thinner crystal. Moreover, in an unambiguous scheme, energy scaling of idler pulses to ~ mJ level is expected via amplification through another, for example, 3-mm BIBO directly pumped by the laser in Fig. 13.

## 5 Conclusions

A homemade capillary fiber system has successfully produced a supercontinuum spanning from 450 to 950 nm, yielding a 3.8 fs pulse after compression. Through cascaded intra-pulse DFG and optical OPA in a single BIBO with CE phase stabilization, a 30 μJ

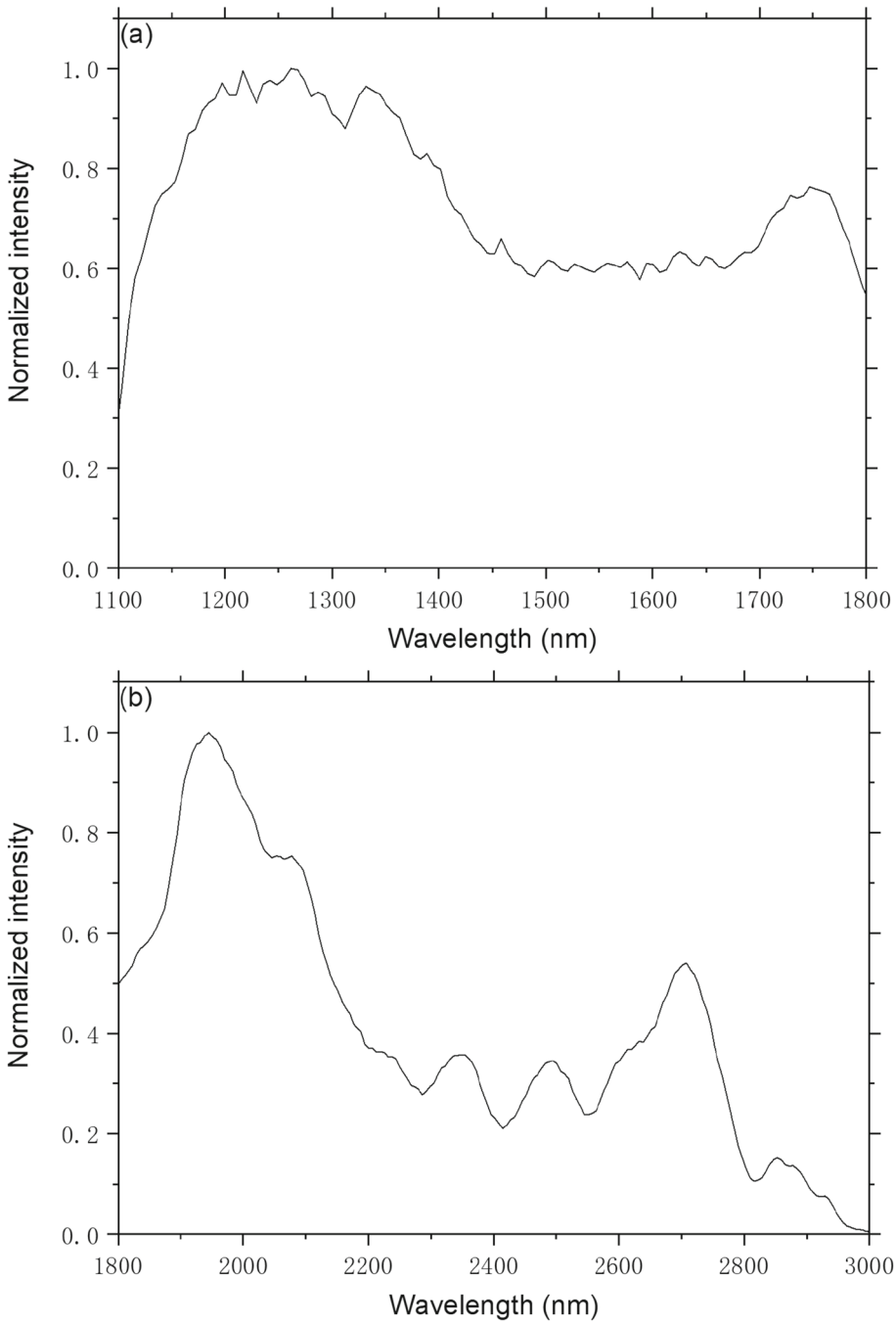


**Fig. 11** The spectra of infrared pulses: **a** the new signal generated in the OPA process; **b** the idler generated in DFA and amplified by OPA

idler pulse spanning from 1800 to 3000 nm was generated, which is beneficial for laser-frequency-comb calibration. In addition, a new signal pulse spanning from 1100 to 1800 nm was obtained via OPA. By using a thinner BIBO, the idler spectrum can be further extended to 5.0 μm. Our methodology addresses three major challenges in astronomical telescope spectrograph calibration simultaneously: achieving broad spectral coverage, stabilizing laser frequency, and attaining pulse energies of approximately μJ. This approach can be implemented with other nonlinear crystals and lead to precise laser-frequency-comb calibration in the near- and mid-infrared domains using a simple and low-cost (thousands of US dollars) setup. With interdisciplinary sciences such as optics, material science, engineering, and physics, astrophotonics is poised to make significant contributions to telescopes and next-generation astronomical instruments. This advancement in supercontinuum generation and frequency comb calibration has the potential to provide high-precision and cost-effective solutions.

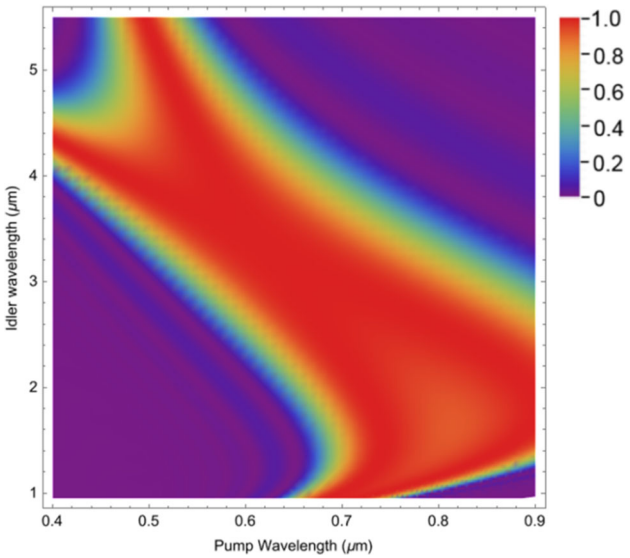


**Fig. 12** The simulated for phase-matching efficiency regarding to pump and idler wavelengths in a 0.3-mm Type I BIBO with a phase-matching angle of 10.6° in the XZ plane

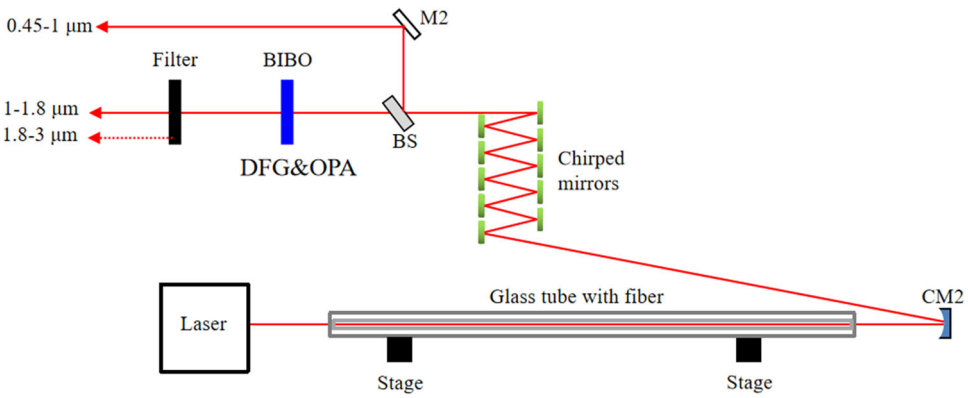


**Fig. 13** The diagram proposed for spectrograph calibration. BS is a beamsplitter used to reflect a fraction of the super continuum from fiber. The dash line indicate the choice of output spectrum by different filters

**Acknowledgements** This work is supported by the funding from National Development and Reform Commission (Q110522S07001, Q110523S07001) and the Fundamental Research Funds for Central Universities (2682020CX77) in China. It is also supported by National Key R&D program of China (2018YFA0404201) and NSFC (12105233).

**Data Availability Statement** This manuscript has associated data in a data repository. [Authors' comment: All data included in this manuscript are available upon reasonable request by contacting with the corresponding author.]

**Declarations**

**Conflict of interest** On behalf of all authors, the corresponding author states that there is no conflict of interest.

## References

1. A. Dinkelaker, A. Rahman, J. Bland-Hawthorn, F. Cantalloube, S. Ellis, P. Feautrier, M. Ireland, L. Labadie, R. Thomson, Astrophotonics: introduction to the feature issue. Appl. Opt. (2021). https://doi.org/10.1364/AO.434555
2. R.P. Butler et al., Attaining doppler precision of 3 m/s. PASP **108**, 500 (1996). https://doi.org/10.1086/133755
3. M.G. Suh, X. Yi, Y.H. Lai et al., Searching for exoplanets using a microresonator astrocomb. Nat. Photon **13**, 25 (2019). https://doi.org/10.1038/s41566-018-0312-3
4. Y. Sun, Wu. Jiayang, M. Tan, Xu. Xingyuan, Y. Li, R. Morandotti, A. Mitchell, D.J. Moss, Applications of optical microcombs. Adv. Opt. Photon. **15**, 86 (2023). https://doi.org/10.1364/AOP.470264
5. A. Quirrenbach et al., CARMENES: Calar Alto high-resolution search for M dwarfs with exo-earths with a near-infrared Echelle spectrograph, Proc. SPIE 7735, Ground-based and Airborne Instrumentation for Astronomy III, (2010) https://doi.org/10.1117/12.857777
6. F. Pepe et al., ESPRESSO at VLT-On-sky performance and first results. Astron. Astrophys. **645**, A96 (2021). https://doi.org/10.1051/0004-6361/202038306
7. A. Marconi., et al., HIRES, the high-resolution spectrograph for the ELT. arXiv preprint arXiv:2011.12317 (2020) https://doi.org/10.18727/0722-6691/5219

8. R. McCracken, J. Charsley, D. Reid, A decade of astrocombs: recent advances in frequency combs for astronomy. Opt. Express **25**, 15058 (2017). https://doi.org/10.1364/OE.25.015058
9. A. Sandage, The change of redshift and apparent luminosity of galaxies due to the deceleration of selected expanding universes. Astrophys. J. **136**, 319 (1962). https://doi.org/10.1086/147385
10. A. Marconi et al., EELT-HIRES the high-resolution spectrograph for the E-ELT, Proc. SPIE 9908, Ground-based and Airborne Instrumentation for Astronomy VI, (2016) https://doi.org/10.1117/12.2231653
11. C. Lovis, M. Mayor, F. Pepe et al., An extrasolar planetary system with three Neptune-mass planets. Nature **441**, 305 (2006). https://doi.org/10.1038/nature04828
12. T. Steinmetz et al., Laser frequency combs for astronomical observations. Science **321**, 1335 (2008). https://doi.org/10.1126/science.1161030
13. M.T. Murphy et al., High-precision wavelength calibration with laser frequency combs. Mon. Not. R. Astron. Soc. **380**, 839 (2007). https://doi.org/10.1111/j.1365-2966.2007.12147.x
14. A. Marandi, N. Leindecker, V. Pervak, R. Byer, K. Vodopyanov, Coherence properties of a broadband femtosecond mid-IR optical parametric oscillator operating at degeneracy. Opt. Express **20**, 7255 (2012). https://doi.org/10.1364/OE.20.007255
15. S.T. Cundiff, Phase stabilization of ultrashort optical pulses. J. Phys. D: Appl. Phys. **35**(8), R43 (2002). https://doi.org/10.1088/0022-3727/35/8/201
16. L. Chen et al., Application of the nitrogen laser calibration system in LAASO-WFCTA. PoS ICRC2021 (2021) https://doi.org/10.22323/1.395.0269
17. I. Hartl, H.A. Mckay, R. Thapa, B.K. Thomas, L. Dong, M.E. Fermann, GHz Yb-femtosecond-fiber laser frequency comb. Conf. Lasers Electro-Opt. (CLEO) (2009). https://doi.org/10.1364/CLEO.2009.CMN1
18. H.-W. Chen, G. Chang, S. Xu, Z. Yang, F.X. Kärtner, 3 GHz, fundamentally mode-locked, femtosecond Yb-fiber laser. Opt. Lett. **37**(17), 3522 (2012). https://doi.org/10.1364/OL.37.003522
19. B. Xu, H. Yasui, Y. Nakajima, Y. Ma, Z. Zhang, K. Minoshima, Fully stabilized 750-MHz Yb:fiber frequency comb. Opt. Express **25**(10), 11910 (2017). https://doi.org/10.1364/OE.25.011910
20. A. Martinez, S. Yamashita, Multi-gigahertz repetition rate passively modelocked fiber lasers using carbon nanotubes. Opt. Express **19**(7), 6155 (2011). https://doi.org/10.1364/OE.25.011910
21. W. Yuanjie., H. Zinan., T. Steinmetz, M. Yeo, K. Stockwald, and R. Holzwarth, 20 GHz astronomical laser frequency comb with super-broadband spectral coverage, Proc. SPIE 12184, Ground-based and Airborne Instrumentation for Astronomy IX, 121841J (2022) https://doi.org/10.1117/12.2624078
22. R.A. McCracken, K. Balskus, Z. Zhang, D.T. Reid, Atomically referenced 1-GHz optical parametric oscillator frequency comb. Opt. Express **23**(12), 16466 (2015). https://doi.org/10.1364/OE.23.016466
23. M. Endo, A. Ozawa, Y. Kobayashi, 6-GHz, Kerr-lens mode-locked Yb:Lu2O3 ceramic laser for combresolved broadband spectroscopy. Opt. Lett. **38**(21), 4502 (2013). https://doi.org/10.1364/OL.38.004502
24. A. Klenner, S. Schilt, T. Südmeyer, U. Keller, Gigahertz frequency comb from a diode-pumped solid-state laser. Opt. Express **22**(25), 31008 (2014). https://doi.org/10.1364/OE.22.031008
25. C.A. Zaugg, A. Klenner, M. Mangold, A.S. Mayer, S.M. Link, F. Emaury, M. Golling, E. Gini, C.J. Saraceno, B.W. Tilma, U. Keller, Gigahertz self-referenceable frequency comb from a semiconductor disk laser. Opt. Express **22**(13), 16445 (2014). https://doi.org/10.1364/OE.22.016445
26. A.R. Johnson et al., Octave-spanning coherent supercontinuum generation in a silicon nitride waveguide. Opt. Lett. **40**, 5117 (2015). https://doi.org/10.1364/OL.40.005117
27. A. Ishizawa, T. Nishikawa, A. Mizutori, H. Takara, A. Takada, T. Sogawa, M. Koga, Phase-noise characteristics of a 25-GHz-spaced optical frequency comb based on a phase- and intensity-modulated laser. Opt. Express **21**(24), 29186 (2013). https://doi.org/10.1364/OE.21.029186
28. K. Beha, D. C. Cole, P. Del'Haye, A. Coillet, S. A. Diddams, and S. B. Papp, Self-referencing a continuouswave laser with electro-optic modulation, arXiv:1507.06344v1 (2015) https://doi.org/10.48550/arXiv.1507.06344
29. K. Kashiwagi, T. Kurokawa, Y. Okuyama, T. Mori, Y. Tanaka, Y. Yamamoto, M. Hirano, Direct generation of 12.5-GHz-spaced optical frequency comb with ultrabroad coverage in near-infrared region by cascaded fiber configuration. Opt. Express **24**(8), 8120–8131 (2016). https://doi.org/10.1364/OE.24.008120
30. T. Xue, L. Dong, He. Jin-ping, Research status and application prospects of astrophotonics. Chin. Astron. Astrophys **47**, 54 (2023). https://doi.org/10.1016/j.chinastron.2023.03.008
31. P. Del'Haye, A. Coillet, T. Fortier, K. Beha, D.C. Cole, K.Y. Yang, H. Lee, K.J. Vahala, S.B. Papp, S.A. Diddams, Phase-coherent microwave-to-optical link with a self-referenced microcomb. Nat. Photonics **10**(8), 516 (2016). https://doi.org/10.1038/nphoton.2016.105
32. A.S. Mayer, A. Klenner, A.R. Johnson, K. Luke, M.R.E. Lamont, Y. Okawachi, M. Lipson, A.L. Gaeta, U. Keller, Frequency comb offset detection using supercontinuum generation in silicon nitride waveguides. Opt. Express **23**(12), 15440 (2015). https://doi.org/10.1364/OE.23.015440
33. E. Obrzud, M. Rainer, A. Harutyunyan et al., A microphotonic astrocomb. Nat. Photon **13**, 31 (2019). https://doi.org/10.1038/s41566-018-0309-y
34. G.G. Ycas, F. Quinlan, S.A. Diddams, S. Osterman, S. Mahadevan, S. Redman, R. Terrien, L. Ramsey, C.F. Bender, B. Botzer, S. Sigurdsson, Demonstration of on-sky calibration of astronomical spectra using a 25 GHz near-IR laser frequency comb. Opt. Express **20**(6), 6631 (2012). https://doi.org/10.1364/OE.20.006631
35. L. Tang, H. Ye, J. Hao, R. Wei, D. Xiao, Design and characterization of a thermally stabilized fiber Fabry-Perot etalon as a wavelength calibrator for high-precision spectroscopy. Appl. Opt. **60**, D1 (2021). https://doi.org/10.1364/AO.417586
36. A.G. Glenday, C.-H. Li, N. Langellier, G. Chang, L.-J. Chen, G. Furesz, A.A. Zibrov, F. Kärtner, D.F. Phillips, D. Sasselov, A. Szentgyorgyi, R.L. Walsworth, Operation of a broadband visible-wavelength astro-comb with a high-resolution astrophysical spectrograph. Optica **2**(3), S1 (2015). https://doi.org/10.1364/OPTICA.2.000250
37. A. Gambetta, R. Ramponi, M. Marangoni, Mid-infrared optical combs from a compact amplified Er-doped fiber oscillator. Opt. Lett. **33**(22), 2671 (2008). https://doi.org/10.1364/OL.33.002671
38. J.C. Boggio, T. Fremberg, D. Bodenmüller, C. Sandin, M. Zajnulina, A. Kelz, D. Giannone, M. Rutowska, B. Moralejo, M.M. Roth, M. Wysmolek, Wavelength calibration with PMAS at 3.5 m Calar Alto Telescope using a tunable astro-comb. Opt. Commun. **15**(415), 186–193 (2018). https://doi.org/10.1016/j.optcom.2018.01.007
39. Y. Cheng, D. Xiao, R. McCracken, D. Reid, Laser-frequency-comb calibration for the extremely large telescope: an OPO-based infrared astrocomb covering the H and J bands. J. Opt. Soc. Am. B **38**, A15 (2021). https://doi.org/10.1364/JOSAB.421310
40. M. Nisoli, S. De Silvestri, O. Svelto, Generation of high energy 10 fs pulses by a new pulse compression technique. Appl. Phys. Lett. **68**, 2793 (1996). https://doi.org/10.1063/1.116609
41. H. Nakatsuka, D. Grischkowsky, A.C. Balant, Nonlinear picosecond-pulse propagation through optical fibers with positive group velocity dispersion. Phys. Rev. Lett. **47**, 910 (1981). https://doi.org/10.1103/PhysRevLett.47.910
42. C. Vozzi, M. Nisoli, G. Sansone et al., Optimal spectral broadening in hollow-fiber compressor systems. Appl. Phys. B **80**, 285 (2005). https://doi.org/10.1007/s00340-004-1721-1

43. G. Tempea, V. Yakovlev, B. Bacovic, F. Krausz, K. Ferencz, Tilted-front-interface chirped mirrors. J. Opt. Soc. Am. B **18**, 1747 (2001). https://doi.org/10.1364/JOSAB.18.001747
44. K.W. DeLong, R. Trebino, J. Hunter, W.E. White, Frequency-resolved optical gating with the use of second-harmonic generation. J. Opt. Soc. Am. B **11**(11), 2206–2215 (1994). https://doi.org/10.1364/JOSAB.11.002206
45. R. Trebino, *Frequency-resolved optical gating: the measurement of ultrashort laser pulses*, 1st edn. (Springer, Berlin, 2000), pp.237–330
46. O.S. Kushnir, Y.V. Burak, O.A. Bevz, I.I. Polovinko, Crystal optical studies of lithium tetraborate. J. Phys.: Condens. Matter. **11**(42), 8313 (1999). https://doi.org/10.1088/0953-8984/11/42/312
47. J. Kroupa, D. Kasprowicz, A. Majchrowski, E. Michalski, M. Drozdowski, Optical properties of bismuth triborate (BIBO) single crystals. Ferroelectrics **318**(1), 77–82 (2005). https://doi.org/10.1080/00150190590966081
48. D. Xue, S. Zhang, Structure and non-linear optical properties of $\beta$-Barium Borate. Acta. Cryst. **54**, 652 (1998). https://doi.org/10.1107/S0108768198004649
49. H. Hellwig, J. Liebertz, L. Bohaty, Linear optical properties of the monoclinic bismuth borate $BiB_3O_6$. J. Appl. Phys. **88**, 240 (2000). https://doi.org/10.1063/1.373647


Springer Nature or its licensor (e.g. a society or other partner) holds exclusive rights to this article under a publishing agreement with the author(s) or other rightsholder(s); author self-archiving of the accepted manuscript version of this article is solely governed by the terms of such publishing agreement and applicable law.